Journal of Alloys and Compounds 842 (2020) 155666

Contents lists available at ScienceDirect

Journal of Alloys and Compounds

journal homepage: http://www.elsevier.com/locate/jalcom

Review

Effect of Ce addition on microstructure evolution and precipitation in Cu-Co-Si-Ti alloy during hot deformation

Yongfeng Geng [a, b, c, d], Yi Zhang [a, b, c, *], Kexing Song [a, b, c, **], Yanlin Jia [e, ***], Xu Li [d], Heinz-Rolf Stock [a, b, c], Honglei Zhou [f], Baohong Tian [a, b, c], Yong Liu [a, b, c], Alex A. Volinsky [g], Xiaohui Zhang [a, b, c], Ping Liu [f], Xiaohong Chen [f]

[a] School of Materials Science and Engineering, Henan University of Science and Technology, Luoyang, 471023, PR China
[b] Provincial and Ministerial Co-construction of Collaborative Innovation Center for Non-ferrous Metal New Materials and Advanced Processing Technology, Henan Province, Luoyang, 471023, PR China
[c] Henan Province Key Laboratory of Nonferrous Materials Science and Processing Technology, Luoyang, 471023, PR China
[d] Center for Advanced Measurement Science, National Institute of Metrology, Beijing, 100029, PR China
[e] College of Materials Science and Engineering, Central South University, Changsha, 410083, China
[f] School of Materials Science and Engineering, Shanghai University of Technology, Shanghai 200000, PR China
[g] Department of Mechanical Engineering, University of South Florida, Tampa, 33620, USA

ARTICLE INFO

Article history:
Received 6 February 2020
Received in revised form
9 May 2020
Accepted 14 May 2020
Available online 28 May 2020

Keywords:
Cu-Co-Si-Ti and Cu-Co-Si-Ti-Ce alloys
Hot compression
Flow stress
Microstructure evolution
DRX mechanism

ABSTRACT

Hot compression tests of the Cu-Co-Si-Ti and Cu-Co-Si-Ti-Ce alloys were carried out on the Gleeble-1500 simulator at 0.001−10 s^{-1} strain rates and 500−900 °C deformation temperatures. Compared with the Cu-Co-Si-Ti alloy, the flow stress of the Cu-Co-Si-Ti-Ce alloy increased under the same deformation conditions. The micro texture of the Cu-Co-Si-Ti and Cu-Co-Si-Ti-Ce alloys were analyzed by EBSD. In addition, the texture of Cu-Co-Si-Ti alloy deformed at 700 and 800 °C is {011} <100> Goss texture and {112} <111> copper texture, respectively. However, the {001} <100> cubic texture and {011} <100> Goss texture in Cu-Co-Si-Ti-Ce alloy deformed at 700 and 800 °C were obtained, respectively. The constitutive equations of Cu-Co-Si-Ti and Cu-Co-Si-Ti-Ce alloys were obtained. The activation energy of Cu-Co-Si-Ti and Cu-Co-Si-Ti-Ce alloys is 500.79 kJ/mol and 539.94 kJ/mol, respectively. The Co_2Si precipitate was found in both the Cu-Co-Si-Ti and Cu-Co-Si-Ti-Ce alloys, while the Co_2Si precipitate of Cu-Co-Si-Ti-Ce alloy is smaller than that of the Cu-Co-Si-Ti alloy. Moreover, the dislocation density of Cu-Co-Si-Ti-Ce alloy is higher than Cu-Co-Si-Ti alloy under the same conditions. Finally, Ce addition increased flow stress and activation energy, and inhibited the dynamic recrystallization, which can be attributed to the higher dislocation density and finer Co_2Si precipitate. The CDRX and DDRX mechanisms are the two main DRX mechanisms for Cu-Co-Si-Ti and Cu-Co-Si-Ti-Ce alloys during hot deformation.

Contents

* Corresponding author. School of Materials Science and Engineering, Henan University of Science and Technology, Luoyang, 471023, PR China.
** Corresponding author. School of Materials Science and Engineering, Henan University of Science and Technology, Luoyang, 471023, PR China.
*** Corresponding author.
E-mail addresses: zhshgu436@163.com, yizhang@haust.edu.cn (Y. Zhang), kxsong123@163.com (K. Song), jiayanlin@126.com (Y. Jia).

https://doi.org/10.1016/j.jallcom.2020.155666
0925-8388/

1. Introduction

As well known, the copper alloys have high conductivity and thermal conductivity, excellent corrosion resistance and good mechanical properties, which are widely used in the lead frames, electrical and electronics industry and so on [1–7]. These excellent properties of copper alloys also attracted a large number of researchers' interests to work in this issue. Lead frames play an essential role in the integrated electrical connection. In recent years, with the development of integrated electrical connection towards to the smaller and better performance, which means the lead frames must meet the performance requirements. In other words, the performance requirements for copper alloys have been increased rapidly. The most commonly methods to improve the properties of copper alloys is the addition of trace alloy elements and rare earth elements in the copper matrix, such as Co [8], Cr [9], Zr [10], Sn [11], Ti [12,13], Ag [14], Ce [5,15] and so on. Through the solution treatment, the alloy elements are melted into the copper matrix to form the supersaturated solid solution. In addition, after the thermal deformation or aging treatment, the alloy elements are separated out in the form of compounds to strengthen the copper matrix, which improves the mechanical properties of the alloy by pinning the dislocations and grain boundaries, and finally meet the performance requirements of lead frames.

Sun et al. [16] investigated the effects of Co and Si additions and cryogenic rolling on the structure and properties of Cu-Cr alloys. The $Cr_{15}Co_9Si_6$ and Co_2Si phases were confirmed with the Co and Si additions into the Cu-Cr alloy according to the microstructure analysis, which can strengthen the matrix and improve the tensile properties of the alloy. Xiao et al. [17] found that the δ-Ni_2Si and $(Ni, Co)_2Si$ precipitates during aging, which the precipitations stimulated by Co can lead to the much higher mechanical property and electrical conductivity. Li et al. [18] investigated the microstructure evolution and properties of a quaternary Cu-Ni-Co-Si alloy with high strength and conductivity, and found that the Ni, Co and Si atoms exhibited a substantial amount of co-segregation in the peak-aged state. Huang et al. [19] obtained much smaller and distributed more densely precipitates by the two-step thermo-mechanical process. Lee et al. [20] investigated the tensile and electrical properties of direct aged Cu-Ni-Si-x%Ti alloys, and found that the tensile strength and electrical conductivity combination with the Ti addition tended to be greater than that without Ti addition. Zhao et al. [21] investigated the optimization of strength and ductility in an as-extruded Cu-15Ni-8Sn alloy by the additions of Si and Ti obtained a superior combination of strength-ductility due to the additions of Si and Ti. Wei et al. [22] investigated effects of Ti content on corrosion behavior of Cu-Ti alloys in 3.5% NaCl solution and the results showed that Ti dissolved in the Cu matrix changes the corrosion process of the alloys. Adnan et al. [23] revealed an increment in the hardness, the yield strength and the maximum strain (e max%) occurred with the increase of the (Ce %) in the Cu-14%Al-4.5%Ni base shape memory alloy. Wang et al. [24] investigated the effects of Ce and Y addition on microstructure evolution and precipitation of Cu-Mg alloy during the hot deformation, and found that the Ce addition can significantly delay the dynamic recrystallization and improve the flow stress and activation energy of Cu-Mg alloy.

Based on the above researches, the precipitation strengthening alloys were obtained by the addition of Co, Si, Ti, and Ce element, respectively. On one hand, there are several investigations on the aging behaviors of Cu-Co-Si alloys, but the hot deformation behavior of Cu-Co-Si alloys has been rarely investigated. On the other hand, the effects of Ti addition on the hot compression behavior of the Cu-Co-Si alloy have been investigated in our previous work [25]. Thus, the effects of Ce addition on the hot compression behavior of the Cu-Co-Si-Ti alloy by hot compression test have been investigated in this paper. The hot compression tests were carried out by using the Gleeble-1500 simulator at 0.001–10 s^{-1} strain rates and 500–900 °C deformation temperatures, respectively. The effects of Ce addition on the flow stress, microstructure evolution, electron backscatter diffraction (EBSD) images and activation energy were compared, respectively, and the precipitates of the Cu-Co-Si-Ti and Cu-Co-Si-Ti-Ce alloys were also analyzed.

2. Experimental materials and procedures

The Cu-Co-Si-Ti and Cu-Co-Si-Ti-Ce alloys used in this experiment were made by vacuum melting with the 99% standard electrolytic cathode copper, pure Co, Si, Cu-45% Ti master alloy and Cu-19% Ce master alloy in the ZG-0.01-40-4 vacuum medium frequency induction furnace. On one hand, the argon was needed to prevent oxygen from entering and causing oxidation during smelting. On the other hand, adding the deoxidizer was necessary in melting process to make the deoxidizer react with impurity elements and form oxides floating on liquid surface. In addition, the crucible for melting is the graphite crucible with the size of internal diameter of ~90 mm, ~20 mm thickness and ~190 mm height. Firstly, put the copper metal block into the furnace, melt it into liquid, and then add other master alloys. The pouring temperature of the experiment was set between 1150 and 1250 °C. Finally, the melted metal slurry was injected into the pre-heated mold (internal diameter of ~90 mm, ~20 mm thickness and ~190 mm height) for cooling. After the ingots were cooled to room temperature, the riser and skin were cut off, and then the next heat treatment can be carried out. The nominal and analyzed composition for the Cu-Co-Si-Ti and Cu-Co-Si-Ti-Ce alloys was listed in Table 1. After solidification, the ingots were annealed at 960 °C for 1 h, and then

Table 1
The nominal and analyzed composition of the alloys.

Nominal composition(wt.%)	Analyzed composition(wt.%)				
	Co	Si	Ti	Ce	Cu
Cu-1Co-0.65Si-0.1Ti	0.895	0.601	0.094	~	Bal.
Cu-1Co-0.65Si-0.1Ti-0.15Ce	0.909	0.596	0.089	0.135	Bal.

extruded into 30 mm diameter bars by the XJ-500 metal profile extrusion machine. In addition, the samples also need to be solution treated at 960 °C for 1 h and then cut into ϕ 8 mm × 12 mm cylinders by wire cutting. Finally, the hot compression tests were carried out on the Gleeble-1500D thermo-mechanical simulator. The hot compression tests were carried out at 500–900 °C temperatures and 0.001–10 s^{-1} strain rates ranges. As for the selection of hot deformation temperature, on one hand, the cracks tend to occur below 500 °C with high strain rates on the basis of practical production. And the hot deformation temperature of Cu-based alloy usually selected as 500–900 °C. On the other hand, according to the Cu-Co phase diagram in our previous paper [25], the phases at room temperature are Cu and ε-Co. Thus, the deformation temperature was selected as 500–900 °C and the strain rate was 0.001 s^1 to 10 s^1.

After the hot deformation, the specimens were cut along the longitudinal plane in order to analyze the microstructure evolution of the Cu-Co-Si-Ti and Cu-Co-Si-Ti-Ce alloys. The microstructure evolution for the two alloys was observed by the Olympus PMG3 optical microscope (OM), JSM-7800F backscatter scanning electron microscope and JEM-2100 transmission electron microscope (TEM), respectively. The etching solution used for the optical microscope observation was 3.5 g $FeCl_3$, 5 ml HCl and 95 ml anhydrous alcohol. After the mechanical polishing and electro-polishing, the samples were observed by the backscatter scanning electron microscope for electron backscatter diffraction (EBSD) observations. The samples with 3 mm diameter and 50 μm thickness were ion thinned by the Gatan 691 ion thinner. After that, the samples were observed by the transmission electron microscope.

3. Results

3.1. Flow stress

The true stress-true strain curves of the Cu-Co-Si-Ti and Cu-Co-Si-Ti-Ce alloys deformed at 0.001 s^{-1}, 0.01 s^{-1}, 0.1 s^{-1} and 1 s^{-1} and the various deformation temperatures from 500 to 900 °C are shown in Fig. 1. In general, there are three typical characteristics in the hot deformation process of alloys: the work hardening, dynamic recovery and dynamic recrystallization [24,26,27]. The flow stress of the alloys increases rapidly to the peak value at the beginning of hot deformation, which represents the characteristic of the work hardening. With the development of the thermal deformation, the flow stress of the alloy decreases to a certain value and remains the stable value or the flow stress still decreases until the end of thermal deformation. The stable value indicates that the work hardening and dynamic softening keep balance during the hot deformation, and the continuous decrease of flow stress indicates that the effect of dynamic recrystallization and dynamic recovery is more obviously in the process of thermal deformation. In addition, the values of the flow stress are mainly affected by the strain rates and deformation temperatures [28–30]. Generally, the flow stress decreases with the increasing of temperature or the decreasing of the strain rate. For instance, the peak stress of the Cu-Co-Si-Ti alloy decreased from 265 MPa to 170 MPa when the temperature increased from 500 to 700 °C at a strain rate of 1 s^{-1}. This is because the average kinetic energy of atoms increases with the increasing of temperature, which reduces the critical slip shear force of the deformed alloy, and makes dislocation movement and thermal diffusion more active. Therefore, the increasing of the deformation temperature promotes the nucleation and growth of dynamic recrystallization grains [31]. Moreover, the peak stress of the Cu-Co-Si-Ti alloy decreased from 220 MPa to 181 MPa with the strain rate decreased from 0.1 s^{-1} to 0.01 s^{-1}, deformed at 600 °C. The reason is that the low strain rate provided sufficient time for dynamic recrystallization, and the degree of dislocation increment was relatively gentle at the low strain rate, so the flow stress of the alloy at lower strain rate was lower.

Compared the flow stress between Cu-Co-Si-Ti alloy and Cu-Co-Si-Ti-Ce alloy, it is obviously that the flow stress of Cu-Co-Si-Ti-Ce alloy is higher than that of Cu-Co-Si-Ti alloy at the same deformation conditions. This may be the addition of Ce promotes the precipitation, refines the precipitated particles pinning at the grain boundaries and dislocations, which hinders the movement of dislocations and grain boundaries. Eventually, the flow stress of the Cu-Co-Si-Ti-Ce alloy increases. Wang et al. [5,24] also agrees with this point.

3.2. Microstructure evolution

3.2.1. Initial microstructure

Fig. 2(a) and (b) show the extruded microstructure of Cu-Co-Si-Ti and Cu-Co-Si-Ti-Ce alloys, respectively. In addition, Fig. 2(c) and (d) show the microstructure of Cu-Co-Si-Ti and Cu-Co-Si-Ti-Ce alloys solution treated at 960 °C for 1 h. It can be seen that the grain size of the Cu-Co-Si-Ti-Ce alloy is relatively smaller than Cu-Co-Si-Ti alloy in the same state.

3.3. Microstructure evolution after hot deformation

The main applications of EBSD are the measurement of orientation and orientation difference, micro-texture analysis, real grain size and so on [32,33]. In order to investigate the texture, grain size, and misorientation angle of the Cu-Co-Si-Ti and Cu-Co-Si-Ti-Ce alloys after the hot deformation, the EBSD datas were obtained from the JSM-7800F backscatter scanning electron microscope. Fig. 3 shows the EBSD images under different deformation conditions of the Cu-Co-Si-Ti and Cu-Co-Si-Ti-Ce alloys. As shown in Fig. 3(a) and (c), there are different amount of the recrystallized grains near the deformed grains, which is the characteristics of typical necklace structure [24,34]. With the increased of deformation temperature (Fig. 3(b) and (d)), the necklace structure disappeared gradually, and the deformed grains were replaced by recrystallized grains, i.e. mixed crystal structure appears, which can indicate that the dynamic recrystallization is promoted by the increase of temperature. Moreover, the average grain size decreased with the temperature increased from 700 to 800 °C for Cu-Co-Si-Ti and Cu-Co-Si-Ti-Ce alloys, respectively, which was illustrated in Fig. 4. It can be attributed that the dynamic recrystallization was more sufficient at the higher temperature, as a result, the deformed grains were gradually replaced by recrystallized grains, and the average grain size decreased. For example, the average grain size of Cu-Co-Si-Ti alloy decreased from 16.3 μm to 14.3 μm with the temperature increased from 700 to 800 °C. Meanwhile, the average grain size of Cu-Co-Si-Ti-Ce alloy decreased from 21.1 μm to 20.6 μm under the same condition. For a same deformation temperature, it can be seen that the average grain size of the Cu-Co-Si-Ti-Ce alloy was larger than Cu-Co-Si-Ti alloy. It may be that the amount of fine dynamic recrystallized grains in Cu-Co-Si-Ti-Ce alloy was significantly less than that in Cu-Co-Si-Ti alloy, so the average grain size of the Cu-Co-Si-Ti-Ce alloy increased slightly.

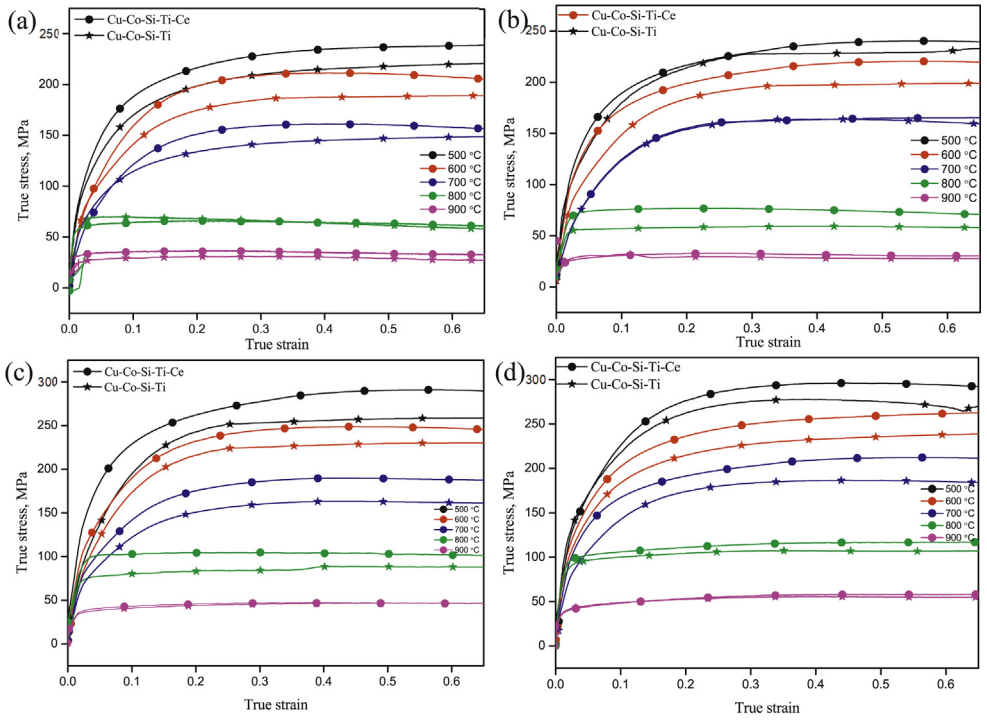

Fig. 1. True stress-True strain curves of Cu-Co-Si-Ti and Cu-Co-Si-Ti-Ce alloys deformed at strain rates of: (a) 0.001 s^{-1}, (b) 0.01 s^{-1}, (c) 0.1 s^{-1}, (d) 1 s^{-1}.

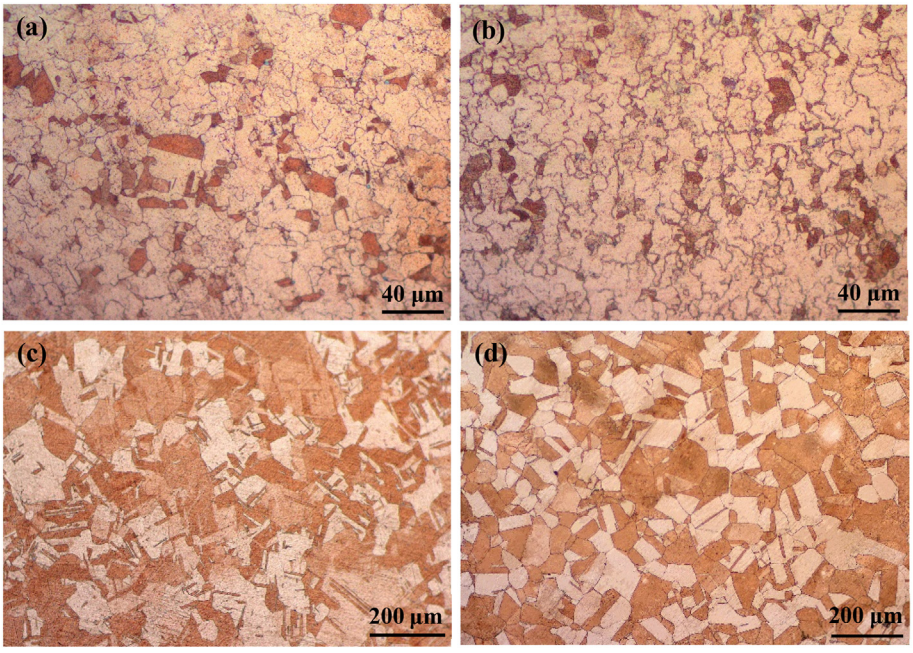

Fig. 2. Microstructure of specimens: extruded at 960 °C (a) Cu-Co-Si-Ti alloy, (b) Cu-Co-Si-Ti-Ce alloy; as solid solution state(c) Cu-Co-Si-Ti alloy, (d) Cu-Co-Si-Ti-Ce alloy.

Therefore, it can be concluded that the addition of Ce delays the dynamic recrystallization of Cu-Co-Si-Ti-Ce alloy.

Fig. 5 shows the EBSD orientation maps and misorientation angles distributions of Cu-Co-Si-Ti and Cu-Co-Si-Ti-Ce alloys deformed at 0.01 s^{-1} and different temperatures. As shown in Fig. 5(a_2-d_2), it can be seen that the distribution of misorientation angles is generally consistent, showing a considerable concentration at the low misorientation angles, which is related to the stored dislocation [35]. There are a great deal of deformed grains and low angle grain boundaries (LAGBs, misorientation angle<15°) for the Cu-Co-Si-Ti and Cu-Co-Si-Ti-Ce alloys deformed at low temperature, as illustrated in Fig. 5(a_2) and (c_2), resulting in the aggregation of dislocations in the deformed grain boundaries and work hardening regions. Generally speaking, the high temperature promotes the dynamic recrystallization. For the same alloy, such as Cu-Co-Si-Ti alloy, the percent of high angle grain boundaries (HAGBs)

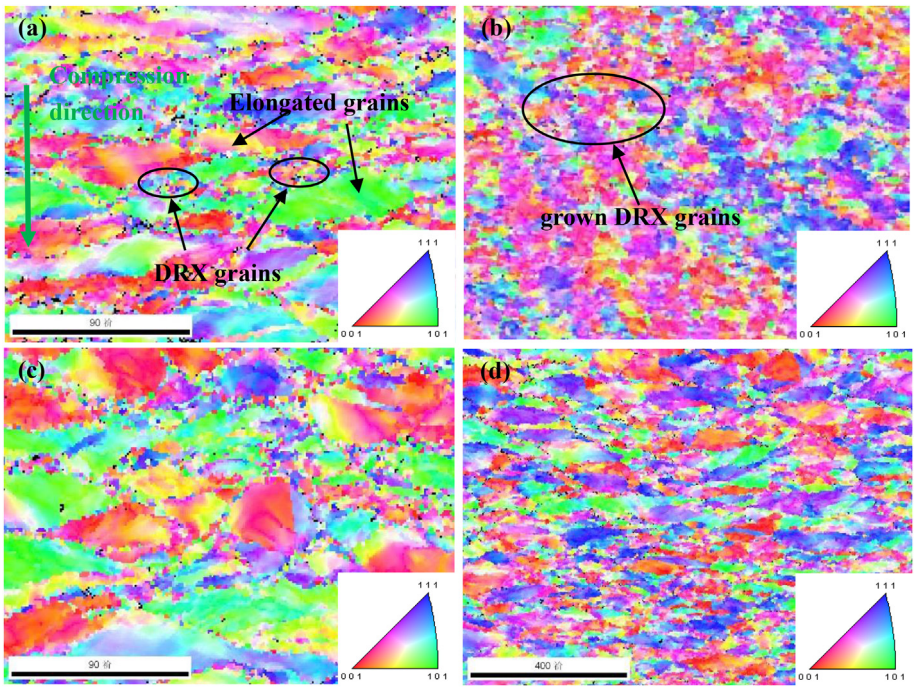

Fig. 3. EBSD images under different deformation conditions: (a) Cu-Co-Si-Ti alloy deformed at 700 °C and 0.01 s^{-1};(b) Cu-Co-Si-Ti alloy deformed at 800 °C and 0.01 s^{-1}; (c) Cu-Co-Si-Ti-Ce alloy deformed at 700 °C and 0.01 s^{-1}; (d) Cu-Co-Si-Ti-Ce alloy deformed at 800 °C and 0.01 s^{-1}.

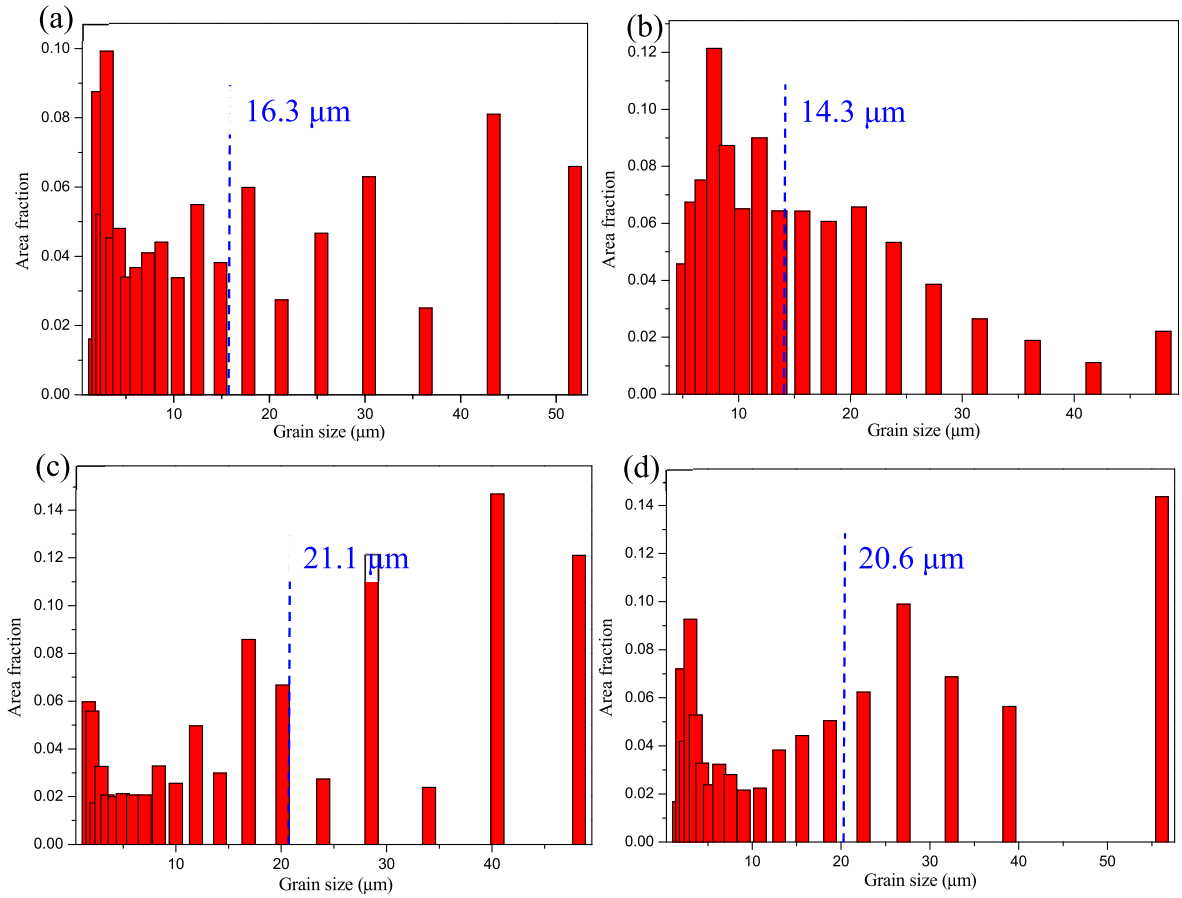

Fig. 4. Grain size distributions under different deformation conditions:(a)Cu-Co-Si-Ti alloy deformed at 700 °C and 0.01 s^{-1};(b)Cu-Co-Si-Ti alloy deformed at 800 °C and 0.01 s^{-1};(c) Cu-Co-Si-Ti-Ce alloy deformed at 700 °C and 0.01 s^{-1};(d)Cu-Co-Si-Ti-Ce alloy deformed at 800 °C and 0.01 s^{-1}.

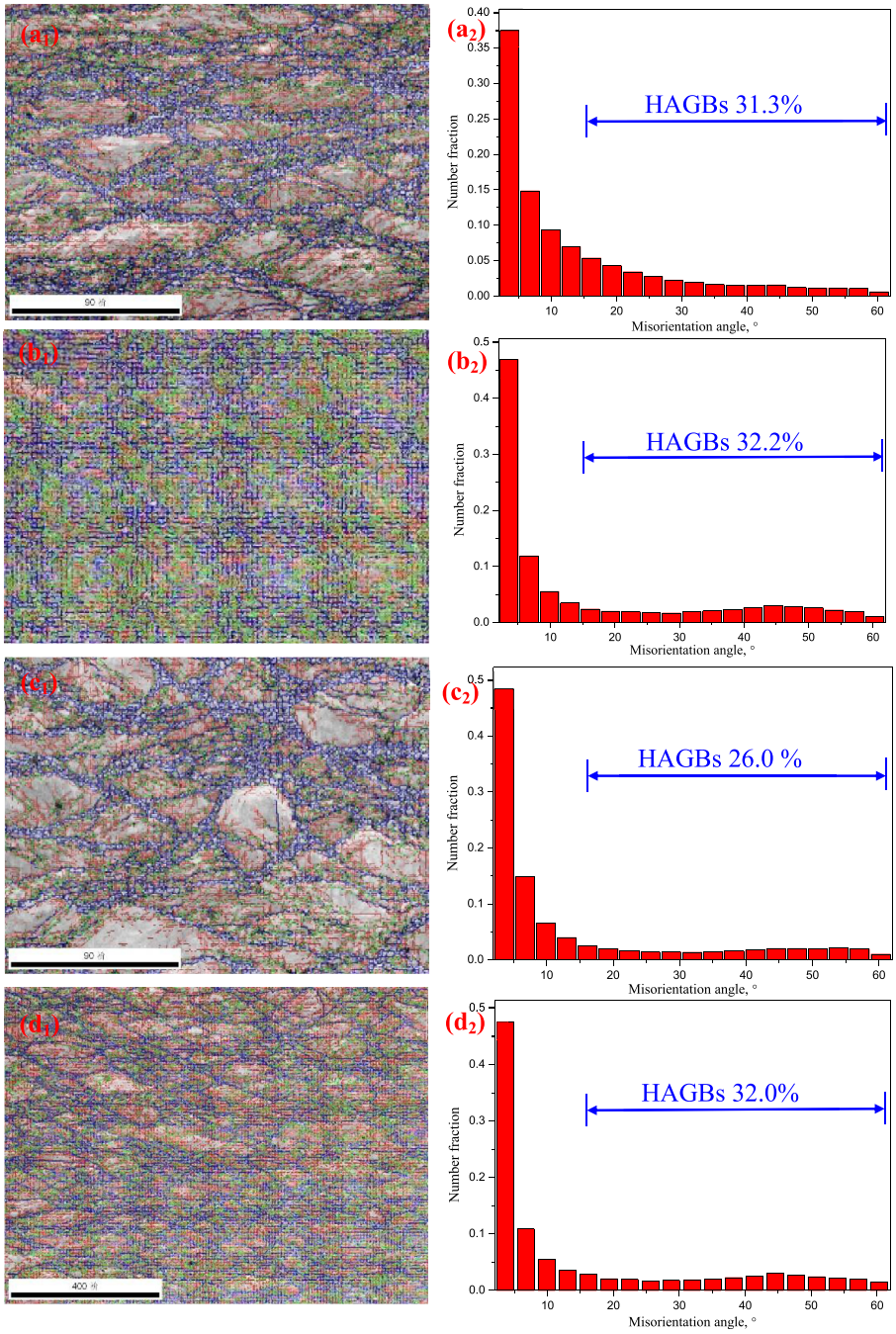

Fig. 5. EBSD orientation maps and misorientation angles distributions of Cu-Co-Si-Ti and Cu-Co-Si-Ti-Ce alloys deformed at 0.01 s^{-1} and different temperatures: (a_1) and (a_2) Cu-Co-Si-Ti alloy deformed at 700 °C; (b_1) and (b_2) Cu-Co-Si-Ti alloy deformed at 800 °C; (c_1) and (c_2) Cu-Co-Si-Ti-Ce alloy deformed at 700 °C; (d_1) and (d_2) Cu-Co-Si-Ti-Ce alloy deformed at 800 °C.

increased from 31.3% to 32.2% with the increased of temperature, which indicated that the enhancement of the dynamic recrystallization due to the increased of temperature can swallow up the stored dislocation [36,37]. The same phenomenon can be observed in Fig. 5(c_2) and (d_2). Therefore, it can be inferred that the increasing of HAGBs means the decreasing of stored dislocation density and the strengthening of dynamic recrystallization. However, it can be seen that the HAGBs of Cu-Co-Si-Ti-Ce alloy are lower than that of the Cu-Co-Si-Ti alloy at the same condition, which can be attributed that there are more deformed grains and higher dislocation density in Cu-Co-Si-Ti-Ce alloy compared with the Cu-Co-Si-Ti alloy. In other words, this phenomenon can be understood as the addition of Ce can enhance the dislocation accumulation which delays the occurrence of DRX.

In order to investigate the texture evolution of Cu-Co-Si-Ti and Cu-Co-Si-Ti-Ce alloys during the hot deformation, the pole figures and inverse pole figures are observed in Fig. 6 and Fig. 7, respectively. For convenience, the pole figures and inverse pole figures are usually represented by the low crystal index, such as {001}, {011} and {111}. In addition, the common recrystallization textures in fcc

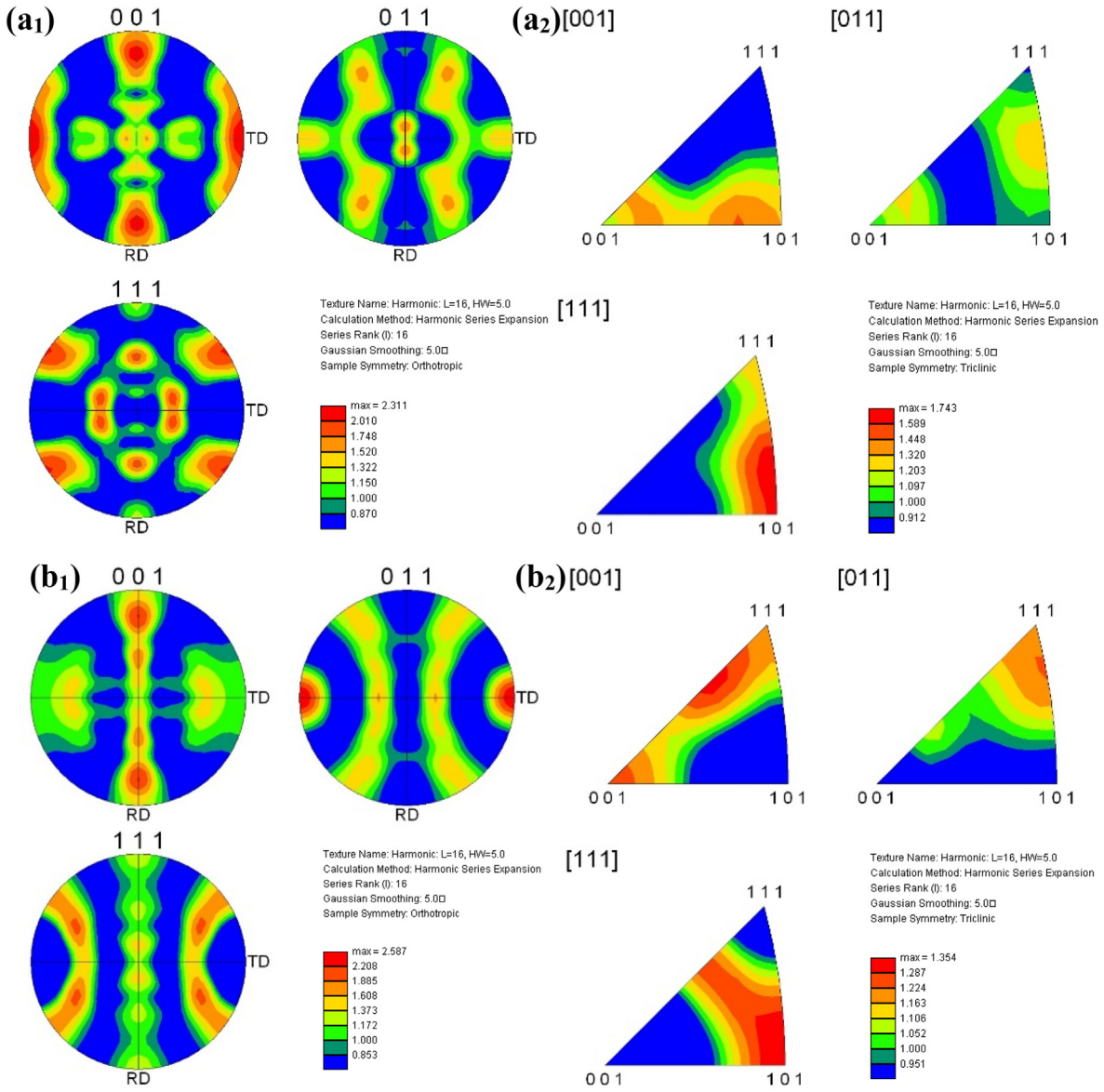

Fig. 6. Pole figures and inverse pole figures of Cu-Co-Si-Ti alloy deformed at 0.01 s^{-1} and different temperatures: (a_1) and (a_2) Cu-Co-Si-Ti alloy deformed at 700 °C; (b_1) and (b_2) Cu-Co-Si-Ti alloy deformed at 800 °C.

metals are the {011} <100> Goss texture, {112} <111> copper texture, {111} <211> R texture, {001} <100> cubic texture and {011} <211> brass texture [38,39]. Fig. 6 shows the pole figures and inverse pole figures of Cu-Co-Si-Ti alloy deformed at 0.01 s^{-1} with the different temperature of 700 °C and 800 °C. The {011} <100> Goss texture was confirmed according to Fig. 6(a_1-a_2). With the increased of temperature to 800 °C, the dynamic recrystallization continued and the {011} <100> Goss texture was gradually substituted by the {112} <111> copper texture, as given in Fig. 6(b_1-b_2). However, the texture of the Cu-Co-Si-Ti-Ce alloy was {001} <100> cubic texture and {011} <100> Goss texture, respectively, compared with the Cu-Co-Si-Ti alloy at the same condition, which can be indicated that the addition of Ce delays the process of dynamic recrystallization. According to the analysis of true-stress and true-strain curves and microstructure evolution, the addition of Ce can inhibit the dynamic recrystallization of the Cu-Co-Si-Ti-Ce alloy, which can be also proved by the texture evolution in Figs. 6 and 7.

3.4. Constitutive equation

It is a process of thermal activation as the metal deforms. In this process, the metal atoms have violent thermal movement, which requires the atoms to cross an energy "threshold" and the energy required is called the deformation activation energy. Meanwhile, the deformation activation energy is an important parameter for evaluating the hot workability of metals. Based on the data of the flow stress curves, the constitutive models of Cu-Co-Si-Ti and Cu-Co-Si-Ti-Ce alloys were established.

According to the model proposed by Sellars and McTegart [40], the relationship between the peak stress, strain rate, and deformation temperature can be described as follows:

$$\dot{\varepsilon} = A\left[\sinh(\alpha\sigma)^n \exp\left(-\frac{Q}{RT}\right)\right] \quad (1)$$

Eq. (1) can be expressed by using the following equations according to the strain magnitude:

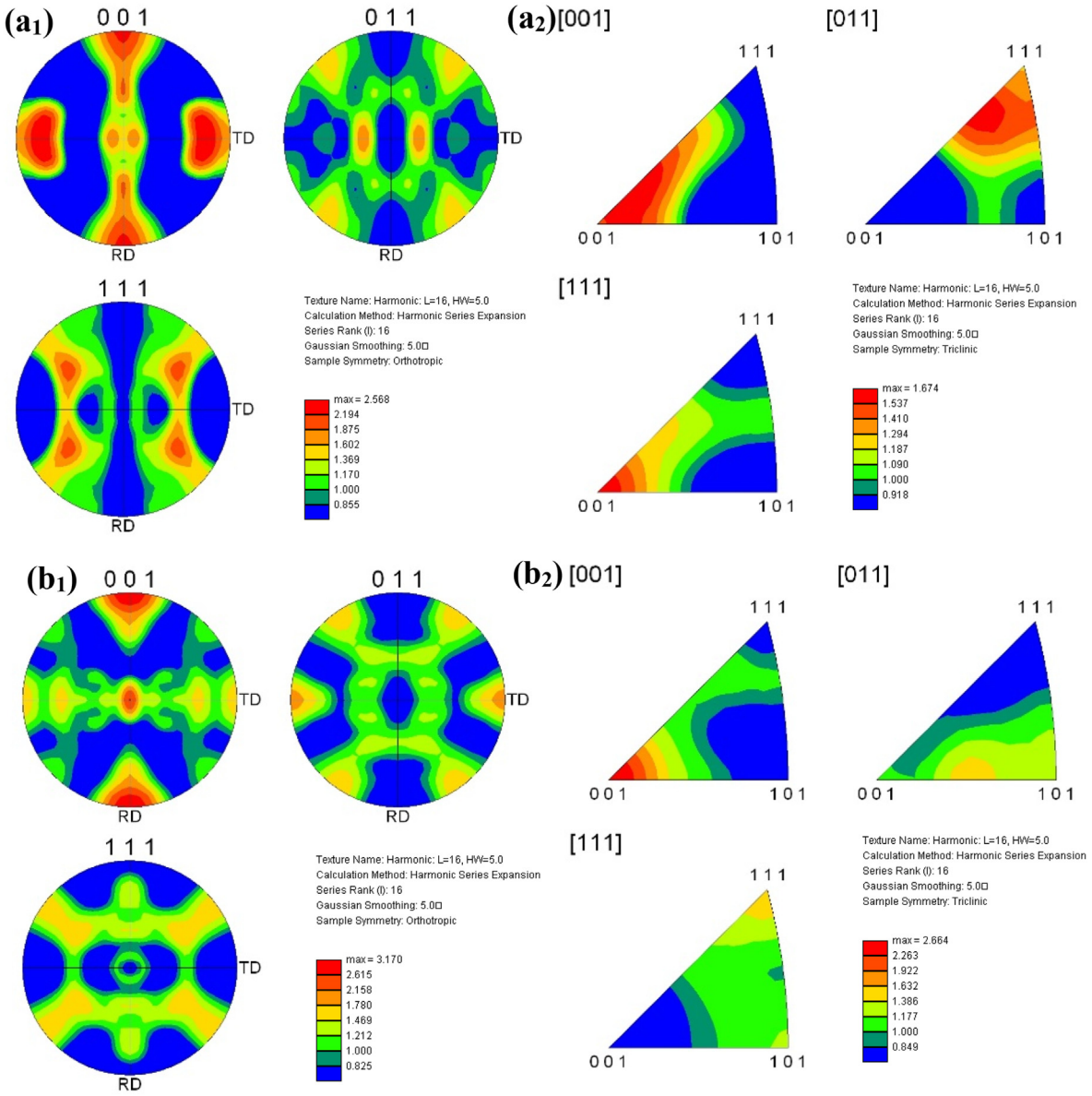

Fig. 7. Pole figures and inverse pole figures of Cu-Co-Si-Ti-Ce alloy deformed at 0.01 s^{-1} and different temperatures: (a_1) and (a_2) Cu-Co-Si-Ti-Ce alloy deformed at 700 °C; (b_1) and (b_2) Cu-Co-Si-Ti-Ce alloy deformed at 800 °C.

$$\dot{\varepsilon} = A_1\sigma^{n_1}\exp\left[-\frac{Q}{RT}\right](\alpha\sigma < 0.8) \tag{2}$$

$$\dot{\varepsilon} = A_2\exp(\beta\sigma)\exp\left[-\frac{Q}{RT}\right](\alpha\sigma < 1.2) \tag{3}$$

Where is the strain rate, σ is the peak stress (MPa), Q is the activation energy (J ▪mol^{-1}), A, A_1, A_2, α, β, n_1, n, and R are constants, and T is the deformation temperature (K).

Taking the natural logarithms of Eqs. (1)–(3):

$$\ln\dot{\varepsilon} = n\ln[\sinh(\alpha\sigma)] - \frac{Q}{RT} + \ln A \tag{4}$$

$$\ln\dot{\varepsilon} = n_1\ln\sigma + \ln A_1 - \frac{Q}{RT} \tag{5}$$

$$\ln\dot{\varepsilon} = \beta\sigma + \ln A_2 - \frac{Q}{RT} \tag{6}$$

Taking partial derivatives of Eq. (1) yields

$$Q = R\left[\frac{\partial(\ln\dot{\varepsilon})}{\partial\ln[\sin\alpha\sigma]}\right]_T\left[\frac{\partial\ln[\sinh\alpha\sigma]}{\partial\left(1/T\right)}\right] = RnS \tag{7}$$

Lattice self-diffusion energy due to the dislocation slip and climb can be expressed in the Zenner parameter [41,42]:

$$Z = \dot{\varepsilon}exp\left[\frac{Q}{RT}\right] \tag{8}$$

Using it in Eq. (1) and taking natural logarithms of both sides gives:

$$\ln Z = \ln A + n[\ln\sinh(\alpha\sigma)] \quad (9)$$

Fig. 8(a–e) show the relationships between ln*(strain rate)* and lnσ, ln*(strain rate)* and σ, ln*(strain rate)* and *ln[*sinh*(*$\alpha\sigma$*)]*, *ln[*sinh*(*$\alpha\sigma$*)]* and $T^{-1} * 10^3\ K^{-1}$ and ln Z and *ln[*sinh*(*$\alpha\sigma$*)]* of Cu-Co-Si-Ti alloy. Meanwhile, n_1, β, n, and S is the average slope of Fig. 8(a–d), which can be determined as $n1 = 19.39$; $\beta = 0.17$; $n = 12.89$; $S = 4.67$, respectively. Therefore, the activation energy of Cu-Co-Si-Ti alloy is Q=R*n*S = 500.79 kJ/mol, and the activation energy of Cu-Co-Si-Ti-Ce alloy is 539.94 kJ/mol by the same way. Fig. 8(d) was obtained by combining Eq. (8) and Eq. (9). The lnA is the intercept of Fig. 8(e), which can be determined as 57.37. Finally, the constitutive equations of the Cu-Co-Si-Ti and Cu-Co-Si-Ti-Ce alloys can be given as follows:

For the Cu-Co-Si-Ti alloy:

$$\dot{\varepsilon} = e^{57.372}[\sinh(0.009\sigma)]^{12.89} exp\left(-\frac{500790}{8.314T}\right)$$

For the Cu-Co-Si-Ti-Ce alloy:

$$\dot{\varepsilon} = e^{64.240}[\sinh(0.008\sigma)]^{13.64} exp\left(-\frac{539940}{8.314T}\right)$$

The activation energy of Cu-Co-Si alloy was determined as 411.65 kJ/mol on the basis of our previous work [25]. Fig. 8(g) shows the activation energy of pure copper, Cu-Co-Si, Cu-Co-Si-Ti and Cu-Co-Si-Ti-Ce alloys. It can be seen that the activation energy of the three alloys is much higher than that of pure copper. Moreover, the activation energy of Cu-Co-Si-Ti-Ce alloy is 23.9% and 7.4% higher than that of Cu-Co-Si and Cu-Co-Si-Ti alloy, respectively, which indicates that the addition of Ti and Ce improve the high temperature stability of Cu-Co-Si alloy. The reason may be that the addition of Ti and Ce promote the precipitation, which can prohibit the movement of dislocations. The specific reasons are discussed as below.

4. Discussion

4.1. Dislocation density

It is well known that the migration of grain boundaries plays an important role in DRX during the hot deformation [43]. The migration of grain boundaries is associated with the dislocations near the grain boundaries. Therefore, it is significant to investigate the dislocation density near the grain boundaries of Cu-Co-Si-Ti and Cu-Co-Si-Ti-Ce alloys. The geometrically necessary dislocation (GND) density is related to the local misorientation, which can be represented as [44,45]:

$$\rho^{GND} = 2\theta \Big/ \mu b \quad (10)$$

Here, ρ^{GND} is the geometrically necessary dislocation (m^{-2}); θ is the average local misorientation (rad), which is defined the critical value of the average local misorientation as 3°. The misorientation angle larger than this value is excluded in the local misorientation calculation since it is caused by the grain boundaries, not by the GND accumulation. μ is the step size in the scanning and b is the Burger's vector (2.55 nm) [25].

Fig. 9 shows the Kernel Average Misorientation (KAM) of Cu-Co-Si-Ti and Cu-Co-Si-Ti-Ce alloys deformed at 0.01 s^{-1} with the temperature of 700 and 800 °C. It can be seen that the geometrically necessary dislocation (GND) of Cu-Co-Si-Ti is 1.0 × 10^{15} m^{-2} and 3.1 × 10^{14} m^{-2}, respectively. And the GND decreased with the increased of temperature, which can prove that the occurrence of DRX sacrifices the dislocation. In addition, the GND of Cu-Co-Si-Ti-Ce alloy is higher than Cu-Co-Si-Ti alloy at the same condition, which can explain why the addition of Ce can improve the stress, activation energy and inhibit the dynamic recrystallization of the Cu-Co-Si-Ti-Ce alloy.

4.2. Precipitates

Fig. 10 shows the microstructure of Cu-Co-Si-Ti alloy deformed at 0.01 s^{-1} and 700 °C. It can be seen that the precipitates have a plate-like shape which have an average size of 12 nm in length and 8 nm in width, as shown in Fig. 10(a) and (b). Fig. 10(c) and (d) shows the Fast Fourier Transform (FFT) pattern and inverse Fast Fourier Transform (IFFT) pattern corresponding to the HRTEM in Fig. 10(b), respectively. The precipitate can be determined to Co_2Si, which has an orthorhombic structure with the lattice parameters of a = 7.109 nm, b = 4.918 nm, c = 3.737 nm, and $\alpha = \beta = \gamma = 90°$. And the zone axis of copper matrix and Co_2Si is $[01\bar{1}]$ and [113], respectively. In addition, it can be seen that the HRTEM image of Co_2Si is clear, and then the diffractive spots after the Fast Fourier Transform (FFT) are even. However, the HRTEM image of copper matrix has only one crystal lattice image in one direction, and only one pair is clear after the Fast Fourier Transform (FFT). The reason is that the observation direction of the precipitate is strictly <113>, but the observation direction of copper matrix is not strictly <110>. As illustrated in Fig. 10(c), the (111) plane of copper is not parallel to the $(30\bar{1})$ plane of Co_2Si, but has an angle difference of 1.45°, which is similar with the calculation result in Yi and Jia [46]. The lattice arrangement directions of $(30\bar{1})_{Co2Si}$, $(2\bar{2}0)_{Co2Si}$, $(\bar{1}2\bar{1})_{Co2Si}$ and $(111)_{Cu}$ are shown in Fig. 10(d). Fig. 10(e) and (f) also is the HRTEM image and FFT of Co_2Si, respectively. The only difference is that the Co_2Si rotates at a certain angle.

Fig. 11 shows the microstructure of Cu-Co-Si-Ti-Ce alloy deformed at 0.01 s^{-1} and 700 °C. It can be seen that the precipitates have a smaller average size of 9 nm in length and 5 nm in width. In addition, a certain number of dislocations are also distributed around the precipitates. The precipitate also has a structure of Co_2Si according to the diffraction spot after the Fast Fourier Transform (FFT), as illustrated in Fig. 11(c). And the zone axis of Cu and Co_2Si is $[0\bar{1}1]_{Cu}$ and $[\bar{1}23]_{Co2Si}$, respectively. It is worth mention that $(111)_{Cu}$ and $(\bar{1}21)_{Co2Si}$ have a 0.86° deviation rather than parallel. The lattice arrangement directions of $(111)_{Cu}$ and $(\bar{1}21)_{Co2Si}$ are illustrated in Fig. 11(d).

Compared with the precipitates of Cu-Co-Si-Ti and Cu-Co-Si-Ti-Ce alloys, as shown in Figs. 10 and 11, respectively. On the one hand, the precipitates size of Cu-Co-Si-Ti-Ce alloy are smaller than that of Cu-Co-Si-Ti alloy. On the other hand, a certain number of dislocations are distributed around the precipitates in Cu-Co-Si-Ti-Ce alloy. According to the above analysis, the interactions between dislocations and precipitates, such as precipitates pinning the dislocations, can explain why the addition of Ce can improve the stress, activation energy and inhibit the dynamic recrystallization of Cu-Co-Si-Ti-Ce alloy.

4.3. Effect of Ce addition on activation energy of hot deformation

Recently, Mirzadeh et al. [47–49] proposed a method that considers the theoretical values of n and Q based on the deformation mechanisms in the constitutive analysis in order to directly deal with the atomic mechanisms. The constant exponent (n) of 13 and self-diffusion activation energy (193 kJ/mol [50]) can be used to describe the appropriate stress, if the deformation mechanism is controlled by the glide and climb of dislocations, which has been

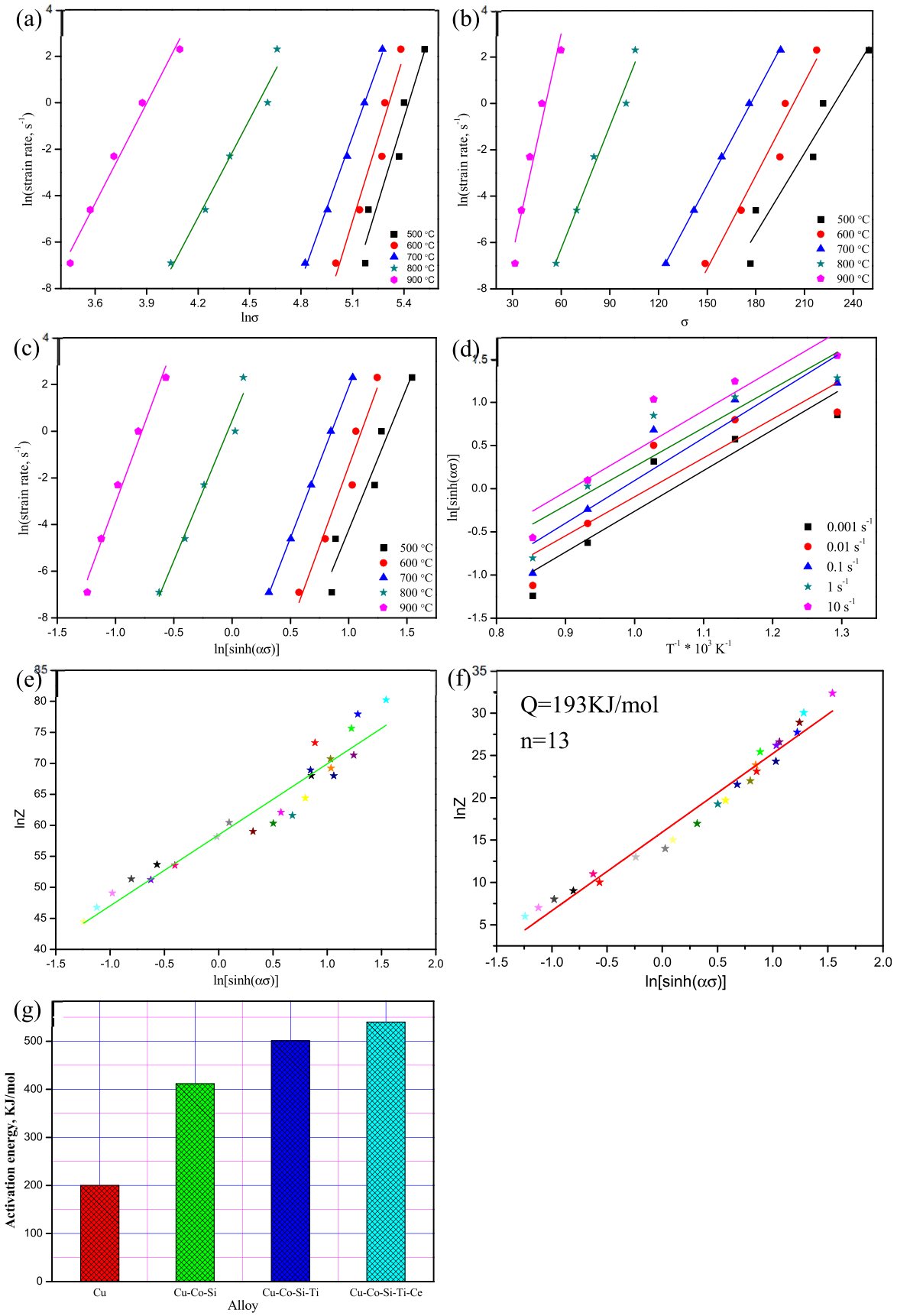

Fig. 8. Relations between: (a) ln(strain rate) and ln σ; (b) ln(strain rate) and σ; (c) ln(strain rate) and ln[sinh(ασ)]; (d) ln[sinh(ασ)] and $T^{-1} * 10^3 K^{-1}$;(e) ln Z and ln[sinh(ασ)]; (f) activation energy of the Cu, Cu-Co-Si, Cu-Co-Si-Ti and Cu-Co-Si-Ti alloys.

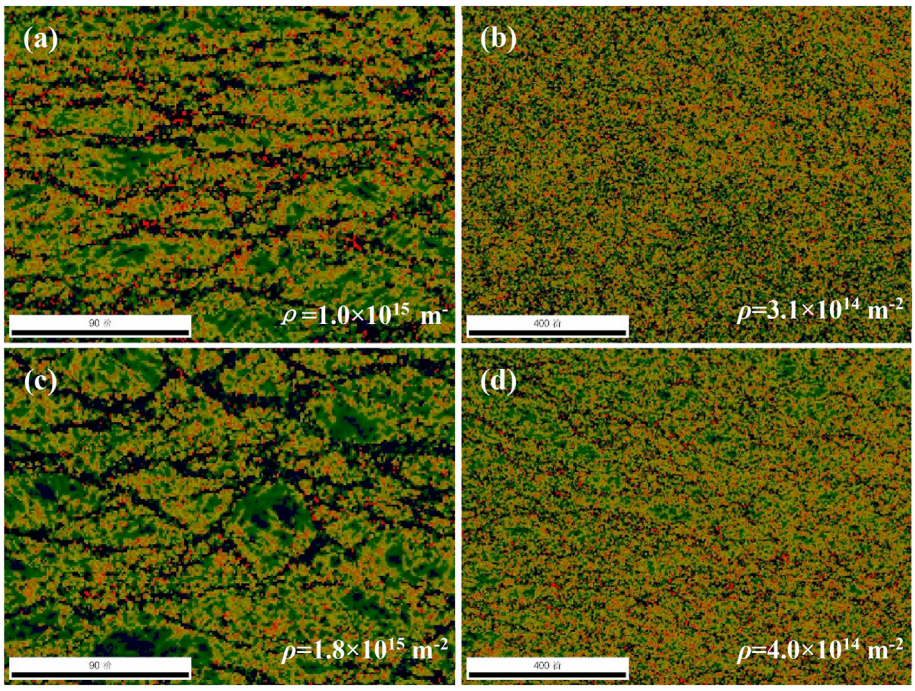

Fig. 9. The Kernel Average Misorientation (KAM) of: (a) Cu-Co-Si-Ti alloy deformed at 700 °C and 0.01 s^{-1}; (b) Cu-Co-Si-Ti alloy deformed at 800 °C and 0.01 s^{-1}; (c) Cu-Co-Si-Ti-Ce alloy deformed at 700 °C and 0.01 s^{-1}; (d) Cu-Co-Si-Ti-Ce alloy deformed at 800 °C and 0.01 s^{-1}.

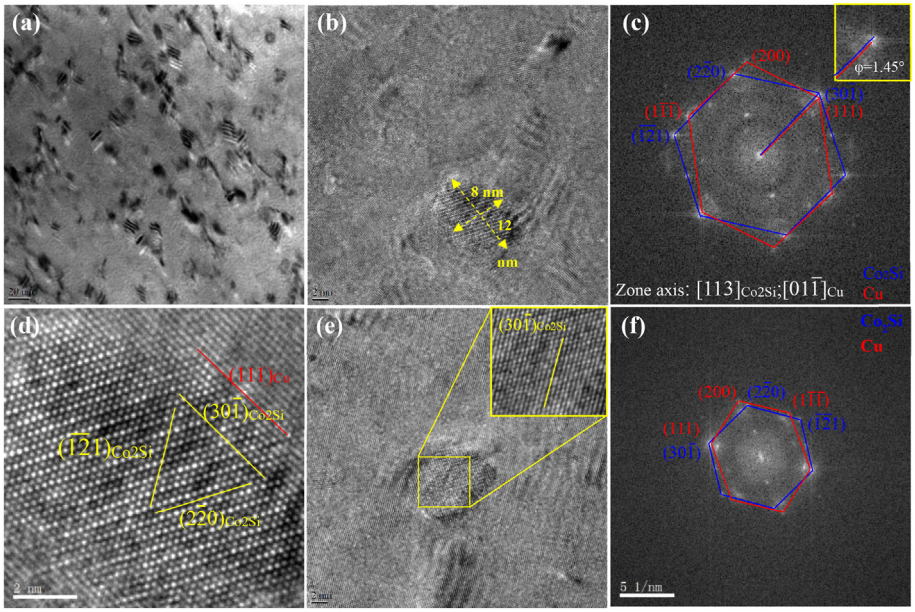

Fig. 10. Microstructure of Cu-Co-Si-Ti alloy deformed at 0.01 s^{-1} and 700 °C:(a) bright field TEM image; (b) and (e) HRTEM; (c) FFT of (b); (d) IFFT of (c); (f) FFT of (e).

proved in Mirzadeh et al. [51] and Wang et al. [5] Therefore, the physically based approach can also describe the effect of rare earth addition on the hot strength in this work. The apparent activation energy of Cu-Co-Si-Ti-Ce alloy is 539.94 kJ/mol due to the Ce addition, moreover, the apparent value of n was 12.89 and 13.64, which are close to the theoretical value of 13. Therefore, it was investigated whether it is possible to consider the values of Q (193 kJ/mol) with n (13) for Cu-Co-Si-Ti and Cu-Co-Si-Ti-Ce alloys and hence elucidating the effect of Ce from the value of the hyperbolic sine constant (A). Based on the hyperbolic sine law and $Z = \dot{\varepsilon}\exp(Q/RT) = A[\sinh(\alpha\sigma)]^n$ [41], the intercept of the plot of ln Z (using $Q = 193$ kJ/mol) against $ln[\sinh(\alpha\sigma)]$ by setting the slope of $n = 13$ can be used for obtaining the values of A. It is still the case of Cu-Co-Si-Ti alloy, and Fig. 8(f) shows the ln Z and $ln[\sinh(\alpha\sigma)]$ of Cu-Co-Si-Ti alloy by $Q = 193$ kJ/mol and $n = 13$. Therefore, the hyperbolic sine constant (A) can be determined as $e^{15.94}$ according to the hyperbolic sine law. The hyperbolic sine constant (A) of Cu-Co-Si-Ti-Ce alloy obtained by the same method is $e^{11.43}$. Finally, the linear regression of the data results for Cu-Co-Si-Ti and Cu-Co-Si-Ti-Ce alloys are as follows:

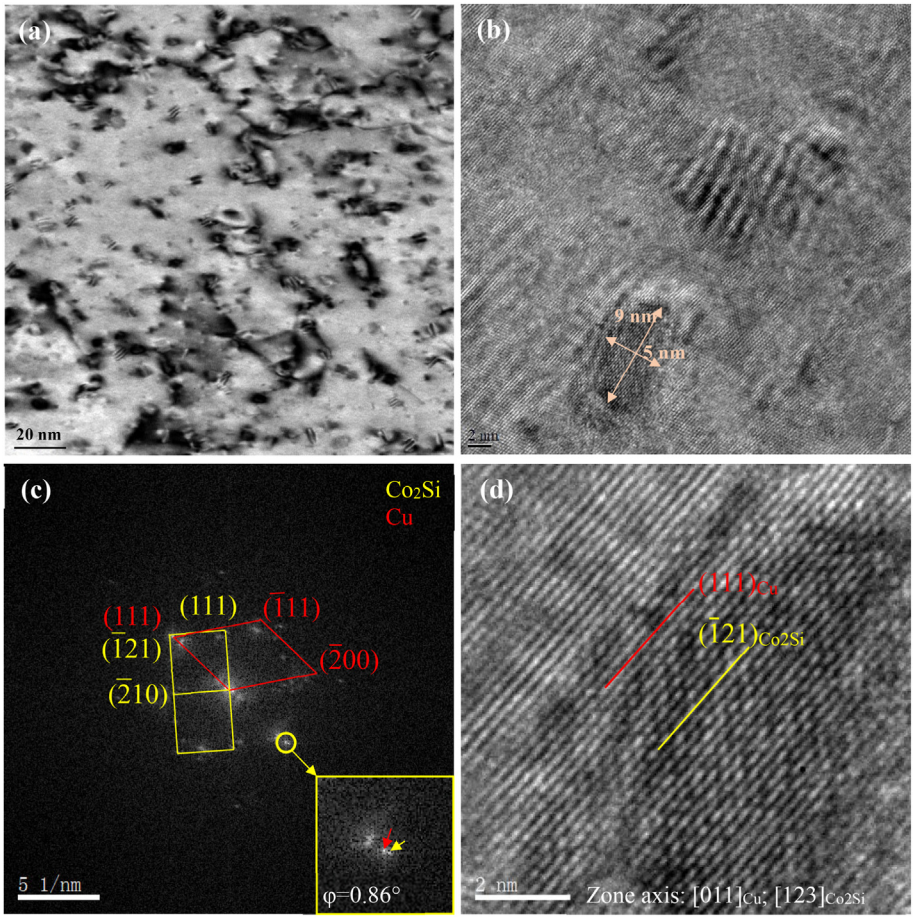

Fig. 11. Microstructure of Cu-Co-Si-Ti-Ce alloy deformed at 0.01 s^{-1} and 700:(a) bright field image; (b) HRTEM; (c) FFT of (b); (d) IFFT of (c).

For the Cu-Co-Si-Ti alloy

$$Z = \dot{\varepsilon}\exp\left(\frac{193000}{8.314T}\right) = e^{15.94}[\sinh(0.009\sigma)]^{13}$$

For the Cu-Co-Si-Ti-Ce alloy

$$Z = \dot{\varepsilon}\exp\left(\frac{193000}{8.314T}\right) = e^{11.43}[\sinh(0.008\sigma)]^{13}$$

It can be seen that the value of the hyperbolic sine constant A (obtained by Fig. 8(f)) is significantly smaller than A (obtained by Fig. 8(e)) for Cu-Co-Si-Ti and Cu-Co-Si-Ti-Ce alloys. In addition, according to the hyperbolic sine law, the flow stress of the material can be expressed as $\sigma = (1/\alpha)[sinh^{-1}(Z/A)^{1/n}]$, which can indicate that it is clear that by decreasing the value of A at a given value of Z, the flow stress increases. Therefore, it shows the magnificent effect of Ce addition on the activation energy of thermal deformation.

As shown in Fig. 8(g), the activation energy of Cu-Co-Si-Ti and Cu-Co-Si-Ti-Ce alloys are higher than Cu-Co-Si alloy due to the addition of Ti and Ce. And the effect of Ti addition on activation energy has been discussed in our previous work [25]. It can be seen that the GND of Cu-Co-Si-Ti-Ce alloy is higher than Cu-Co-Si-Ti alloy at the same condition, as illustrated in Section 4.1. Moreover, it can be also inferred that the precipitates size of Cu-Co-Si-Ti-Ce alloy are smaller than that of Cu-Co-Si-Ti alloy, as illustrated in Section 4.2. And the precipitates are more widely distributed in Cu-Co-Si-Ti-Ce alloy. The effects of hindering grain boundary migration are more significant for Cu-Co-Si-Ti-Ce alloy with the higher GND and smaller precipitates, and makes the process of plastic deformation more difficult, which can explain the reason of higher flow stress and activation energy of thermal deformation for Cu-Co-Si-Ti-Ce alloy than Cu-Co-Si-Ti alloy.

4.4. DRX mechanism

Fig. 12 shows the schematic illustration of the True Stress-True Strain curves and the corresponding microstructure for copper alloy. Generally speaking, there are three stages (work hardening, DRV and DRX) during hot deformation. As given in Fig. 12(a), the dislocation cells were formed due to the increase of deformation degree in the early stage of deformation. With the further hot deformation, the dislocation cells gradually turned into the sub grains. Finally, new DRX grains with HAGBs were formed by progressing sub grains rotation in order to reduce the surface energy of copper alloy, which is consistent with the characteristics of the continuous dynamic recrystallization (CDRX) [30,52]. It can be seen that the dislocations rearrange near the grain boundaries in order to reduce the stress concentration under the early stage of deformation, as shown in Fig. 12(b). And then some original grain boundaries were bulging due to the difference of dislocations near the grain boundaries. Sub grains were formed near the grain boundaries with the further deformation. Finally, the DRX grains can be observed in the stage III with low dislocation density. As stated above and noted that the emergence of such grain boundary morphology confirms that the dynamic recrystallization mechanism of copper alloy is discontinuous dynamic recrystallization

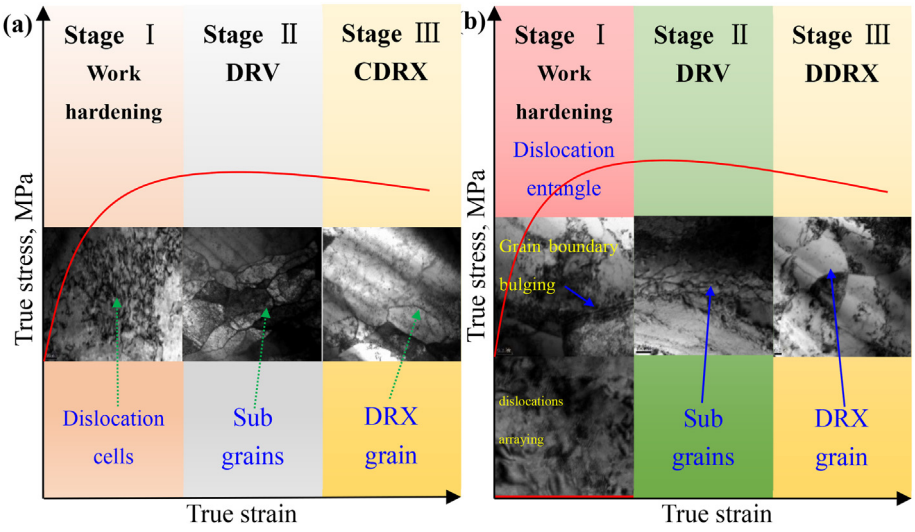

Fig. 12. Schematic illustration of the True Stress-True Strain curves and the corresponding. DRX mechanisms for copper alloy: (a) CDRX; (b) DDRX.

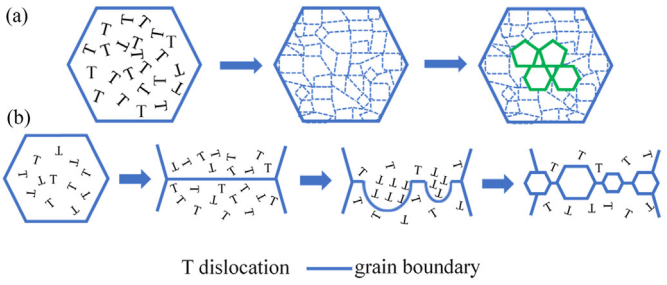

Fig. 13. Schematic diagram of the CDRX (a) and DDRX (b) mechanism.

(DDRX) [53]. From above the analysis, the DRX mechanisms of copper alloy are dominated by CDRX and DDRX. The schematic diagrams of the CDRX mechanism and DDRX mechanism are illustrated in Fig. 13 (a) and (b), respectively.

5. Conclusions

The hot compression test of the Cu-Co-Si-Ti and Cu-Co-Si-Ti-Ce alloys were carried out by using the Gleeble-1500 simulator at 0.001–10 s^{-1} strain rates and 500–900 °C deformation temperatures. The effects of Ce addition on the microstructure evolution were discussed. Several conclusions can be drawn as follows:

(1) The addition of Ce can increase the flow stress of the Cu-Co-Si-Ti-Ce alloy.

(2) The micro texture of the Cu-Co-Si-Ti and Cu-Co-Si-Ti-Ce alloys were analyzed by EBSD. The texture of Cu-Co-Si-Ti alloy deformed at 700 °C and 800 °C is {011} <100> Goss texture and {112} <111> copper texture, respectively. However, there are {001} <100> cubic texture and {011} <100> Goss texture in Cu-Co-Si-Ti-Ce alloy deformed at 700 °C and 800 °C.

(3) The constitutive equations of Cu-Co-Si-Ti and Cu-Co-Si-Ti-Ce alloys were obtained. And the activation energy of Cu-Co-Si–Ti and Cu-Co-Si-Ti-Ce alloys is 500.79 kJ/mol and 539.94 kJ/mol, respectively.

(4) The Co_2Si precipitate was found in both the Cu-Co-Si-Ti and Cu-Co-Si-Ti-Ce alloys, while the Co_2Si precipitate of Cu-Co-Si-Ti-Ce alloy is finer than the Cu-Co-Si-Ti alloy. Moreover, the dislocation density of Cu-Co-Si-Ti-Ce alloy is higher than the Cu-Co-Si-Ti alloy under the same condition.

(5) The DRX mechanisms of Cu-Co-Si-Ti and Cu-Co-Si-Ti-Ce alloys were discussed. And the CDRX and DDRX mechanisms are the two dominated DRX mechanisms.

Declaration of competing interest

The authors declare that they have no known competing financial interests or personal relationships that could have appeared to influence the work reported in this paper.

Acknowledgments

This work was supported by the Open Cooperation Project of Science and Technology of the Henan Province (182106000018), Henan University Scientific and Technological Innovation Talent Support Program (18HASTIT024) and the National Natural Science Foundation of China (U1704143).

References

[1] A.K. Shukla, S.V.S. Narayana Murty, S.C. Sharma, K. Mondal, Constitutive modeling of hot deformation behavior of vacuum hot pressed Cu-8Cr-4Nb alloy, Mater. Des. 75 (2015) 57–64.
[2] W. Wang, H.J. Kang, Z.N. Chen, Z.J. Chen, C.L. Zou, R.G. Li, G.M. Yin, T.M. Wang, Effects of Cr and Zr additions on microstructure and properties of Cu-Ni-Si alloys, Mater. Sci. Eng., A 673 (2016) 378–390.
[3] Y. Zhang, B.H. Tian, P. Liu, High temperature deformation behavior and microstructure preparation of Cu-Ni-Si-P alloy, Mater. Sci. Forum 704–705 (2012) 135–140.
[4] Z.L. Zhao, Z. Xiao, Z. Li, W.T. Qiu, H.Y. Jiang, Q. Lei, Z.R. Liu, Y.B. Jiang, S.J. Zhang, Microstructure and properties of a Cu-Ni-Si-Co-Cr alloy with high strength and high conductivity, Mater. Sci. Eng., A 759 (2019) 396–403.
[5] B.J. Wang, Y. Zhang, B.H. Tian, J.C. An, Alex A. Volinsky, H.L. Sun, Y. Liu, K.X. Song, Effects of Ce addition on the Cu-Mg-Fe alloy hot deformation behavior, Vacuum 155 (2018) 594–603.
[6] Y. Zhang, H.L. Sun, Alex A. Volinsky, B.H. Tian, K.X. Song, B.J. Wang, Y. Liu, Hot workability and constitutive model of the Cu-Zr-Nd alloy, Vacuum 146 (2017) 35–43.
[7] Y.L. Jia, M.P. Wang, C. Chen, Q.Y. Dong, S. Wang, Z. Li, Orientation and diffraction patterns of d-Ni2Si precipitates in Cu-Ni-Si alloy, J. Alloys Compd. 557 (2013) 147–151.
[8] Z. Zhao, Y. Zhang, B.H. Tian, Y.L. Jia, Y. Liu, K.X. Song, Alex A. Volinsky, Co effects on Cu-Ni-Si alloys microstructure and physical properties, J. Alloys Compd. 797 (2019) 1327–1337.
[9] X.L. Guo, Z. Xiao, W.T. Qiu, Z. Li, Z.Q. Zhao, X. Wang, Y.B. Jiang, Microstructure and properties of Cu-Cr-Nb alloy with high strength, high electrical conductivity and good softening resistance performance at elevated temperature,

Mater. Sci. Eng., A 749 (2019) 281–290.
[10] A.H. Huang, Y.F. Wang, M.S. Wang, L.Y. Song, Y.S. Li, L. Gao, C.X. Huang, Y.T. Zhu, Optimizing the strength, ductility and electrical conductivity of a Cu-Cr-Zr alloy by rotary swaging and aging treatment, Mater. Sci. Eng., A 746 (2019) 211–216.
[11] B.M. Luo, D.X. Li, C. Zhao, Z. Wang, Z.Q. Luo, W.W. Zhang, A low Sn content Cu-Ni-Sn alloy with high strength and good ductility, Mater. Sci. Eng., A 746 (2019) 154–161.
[12] J.H. Yuan, L.K. Gong, W.Q. Zhang, B. Zhang, H.G. Wei, X.P. Xiao, H. Wang, B. Yang, Work softening behavior of Cu-Cr-Ti-Si alloy during cold deformation, J Mater. Res. Technol. 8 (2) (2019) 1964–1970.
[13] B. Zhao, T.Y. Y, W.F. Ding, L.C. Zhang, H.H. Su, Z.Z. Chen, Effect of micropores on the microstructure and mechanical properties of porous Cu-Sn-Ti composites, Mater. Sci. Eng., A 730 (2018) 345–354.
[14] S. Xu, H.d. Fu, Y.T. Wang, J.X. Xie, Effect of Ag addition on the microstructure and mechanical properties of Cu-Cr alloy, Mater. Sci. Eng., A 726 (2018) 208–214.
[15] Y. Zhang, Alex A. Volinsky, Hai T. Tran, Z. Chai, P. Liu, B.H. Tian, Y. Liu, Aging behavior and precipitates analysis of the Cu-Cr-Zr-Ce alloy, Mater. Sci. Eng., A 650 (2016) 248–253.
[16] X.L. Sun, J.C. Jie, P.F. Wang, B.L. Qin, X.D. Ma, T.M. Wang, T.J. Li, Effects of Co and Si additions and cryogenic rolling on structure and properties of Cu-Cr alloys, Mater. Sci. Eng., A 740–741 (2019) 165–173.
[17] X.P. Xiao, Z.Y. Yi, T.T. Chen, R.Q. Liu, H. Wang, Suppressing spinodal decomposition by adding Co into Cu-Ni-Si alloy, J. Alloys Compd. 660 (2016) 178–183.
[18] J. Li, G.J. Huang, X.J. Mi, L.J. Peng, H.F. Xie, Y.L. Kang, Microstructure evolution and properties of a quaternary Cu-Ni-Co-Si alloy with high strength and conductivity, Mater. Sci. Eng., A 766 (2019), 138390.
[19] J.Z. Huang, Z. Xiao, J. Dai, Z. Li, H.Y. Jiang, W. Wang, X.X. Zhang, Microstructure and properties of a novel Cu-Ni-Co-Si-Mg alloy with super-high strength and conductivity, Mater. Sci. Eng., A 744 (2019) 754–763.
[20] E.Y. Lee, K.J. Euh, S.Z. Han, S.W. Lim, J.Y. Lee, S.S. Kim, Tensile and electrical properties of direct aged Cu-Ni-Si-x%Ti alloys, Met. Mater. Int. 19 (2013) 183–188.
[21] C. Zhao, Z. Wang, D.X. Li, D.Q. Pan, B.M. Lou, Z.Q. Luo, W.W. Zhang, Optimization of strength and ductility in an as-extruded Cu-15Ni-8Sn alloy by the additions of Si and Ti, J. Alloys Compd. 823 (2020), 153759.
[22] H. Wei, L.F. Hou, Y.C. Cui, Y.Y. Wei, Effect of Ti content on corrosion behavior of Cu–Ti alloys in 3.5% NaCl solution, Trans. Nonferrous Metals Soc. China 28 (2018) 669–675.
[23] R.S.A. Adnan, M.K. Abbass, M.M. AlKubaisy, Effect of Ce addition on mechanical properties and shape memory effect of Cu-14%Al-4.5%Ni shape memory alloy, Mater. Today: SAVE Proc. 20 (2020) 452–460.
[24] B.J. Wang, Y. Zhang, B.H. Tian, V. Yakubov, J.C. An, Alex A. Volinsky, Y. Liu, K.X. Song, L.H. Li, M. Fu, Effects of Ce and Y addition on microstructure evolution and precipitation of Cu-Mg alloy hot deformation, J. Alloys Compd. 781 (2019) 118–130.
[25] Y.F. Geng, X. Li, H.L. Zhou, Y. Zhang, Y.L. Jia, B.H. Tian, Y. Liu, Alex A. Volinsky, X.H. Zhang, K.X. Song, G.X. Wang, L.H. Li, J.R. Hou, Effect of Ti addition on microstructure evolution and precipitation in Cu-Co-Si alloy during hot deformation, J. Alloys Compd. 821 (2020), 153518.
[26] C. Roucoules, M. Pietrzyk, P.D. Hodgson, Analysis of work hardening and recrystallization during the hot working of steel using a statistically based internal variable model, Mater. Sci. Eng. 339 (2003) 1–9.
[27] Y.Q. Ning, X. Luo, H.Q. Liang, H.Z. Guo, J.L. Zhang, K. Tan, Competition between dynamic recovery and recrystallization during hot deformation for TC18 titanium alloy, Mater. Sci. Eng. 635 (2015) 77–85.
[28] Z.Y. Dong, S.G. Jia, P.F. Zhao, M. Deng, K.X. Song, Hot deformation behavior of Cu-0.6Cr-0.03Zr alloy during compression at elevated temperatures, Mater. Sci. Eng. 570 (2013) 87–91.
[29] G.L. Ji, G. Yang, L. Li, Q. Li, Modeling constitutive relationship of Cu-0.4 Mg alloy during hot deformation, J. Mater. Eng. Perform. 23 (2014) 1770–1779.
[30] W.L. Cheng, Y. Bai, S.C. Ma, L.F. Wang, H.X. Wang, H. Yu, Hot deformation behavior and workability characteristic of a fine-grained Mg-8Sn-2Zn-2Al alloy with processing map, J. Mater. Sci. Technol. 35 (2019) 1198–1209.
[31] N. Tahreen, D.F. Zhang, F.S. Pan, X.Q. Jiang, D.Y. Li, D.L. Chen, Hot deformation and processing map of an as-extruded Mg-Zn-Mn-Y alloy containing I and W phases, Mater. Des. 87 (2015) 245–255.
[32] R. Mishnev, I. Shakhova, A. Belyakov, R. Kaibyshev, Deformation microstructures, strengthening mechanisms, and electrical conductivity in a Cu-Cr-Zr alloy, Mater. Sci. Eng., A 629 (2015) 29–40.
[33] F. Bittner, S. Yin, A. Kauffmann, J. Freudenberger, H. Klauß, G. Korpala, R. Kawalla, W. Schillinger, L. Schultz, Dynamic recrystallisation and precipitation behavior of high strength and highly conducting Cu-Ag-Zr alloys, Mater. Sci. Eng., A 597 (2014) 139–147.
[34] J. Liu, X.H. Wang, J.T. Liu, Y.F. Liu, H.Y. Li, C. Wang, Hot deformation and dynamic recrystallization behavior of Cu-3Ti-3Ni-0.5Si alloy, J. Alloys Compd. 782 (2019) 224–234.
[35] W.J. He, A. Chapuis, X. Chen, Q. Liu, Effect of loading direction on the deformation and annealing behavior of a zirconium alloy, Mater. Sci. Eng., A 734 (2018) 364–373.
[36] S.H. Liu, Q.L. Pan, M.J. Li, X.D. Wang, X. He, X.Y. Li, Z.W. Peng, J.P. Lai, Microstructure evolution and physical-based diffusion constitutive analysis of Al-Mg-Si alloy during hot deformation, Mater. Des. 184 (2019), 108181.
[37] G.A. He, Y.F. Zhao, B. Gan, X.F. Sheng, Y. Liu, L.M. Tan, Mechanism of grain refinement in an equiatomic medium-entropy alloy CrCoNi during hot deformation, J. Alloys Compd. 815 (2020), 152382.
[38] C. Haase, L.A. Barrales-Mora, Influence of deformation and annealing twinning on the microstructure and texture evolution of face-centered cubic high-entropy alloys, Acta Mater. 150 (2018) 88–103.
[39] Q. Lei, Z. Li, W.P. Hu, Y. Liu, C.L. Meng, B. Derby, W. Zhang, Microstructure evolution and hardness of an ultra-high strength Cu-Ni-Si alloy during thermo-mechanical processing, J. Mater. Eng. Perform. 25 (2016) 2615–2625.
[40] C.M. Sellars, W.J. McTegart, On the mechanism of hot deformation, Acta Metall. 14 (1966) 1136–1138.
[41] H. Mirzadeh, Constitutive analysis of Mg-Al-Zn magnesium alloys during hot deformation, Mech. Mater. 77 (2014) 80–85.
[42] H. Mirzadeh, Quantification of the strengthening effect of reinforcements during hot deformation of aluminum-based composites, Mater. Des. 65 (2015) 80–82.
[43] A.S.H. Kabir, M. Sanjari, J. Su, I.-H. Jung, S. Yue, Effect of strain-induced precipitation on dynamic recrystallization in Mg-Al-Sn alloys, Mater. Sci. Eng., A 616 (2014) 252–259.
[44] Y.S. Wu, X.Z. Qin, C.S. Wang, L.Z. Zhou, Influence of phosphorus on hot deformation microstructure of a Ni-Fe-Cr based alloy, Mater. Sci. Eng., A 768 (2019), 138454.
[45] Y.S. Wu, Z. Liu, X.Z. Qin, C.S. Wang, L.Z. Zhou, Effect of initial state on hot deformation and dynamic recrystallization of Ni-Fe based alloy GH984G for steam boiler applications, J. Alloys Compd. 795 (2019) 370–384.
[46] J. Yi, Y.L. Jia, Y.Y. Zhao, Z. Xiao, K.J. He, Q. Wang, M.P. Wang, Z. Li, Precipitation behavior of Cu-3.0Ni-0.72Si alloy, Acta Mater. 166 (2019) 261–270.
[47] H. Mirzadeh, J.M. Cabrera, A. Najafizadeh, Constitutive relationships for hot deformation of austenite, Acta Mater. 59 (2011) 6441–6448.
[48] H. Mirzadeh, Quantification of the strengthening effect of rare earth elements during hot deformation of Mg-Gd-Y-Zr magnesium alloy, J. Mater. Res. Technol. 5 (1) (2016) 1–4.
[49] H. Mirzadeh, Constitutive behaviors of magnesium and Mg-Zn-Zr alloy during hot deformation, Mater. Chem. Phys. 152 (2015) 123–126.
[50] Z.T. Wang, R.Z. Tian, Copper Alloy and its Processing Manual, vol. 2, Central South University Press, Hunan, China, 2002, p. 11 (In Chinese).
[51] H. Mirzadeh, M. Roostaei, M.H. Parsa, R. Mahmudi, Rate controlling mechanisms during hot deformation of Mg-3Gd-1Zn magnesium alloy: dislocation glide and climb, dynamic recrystallization, and mechanical twinning, Mater. Des. 68 (2015) 228–231.
[52] Q.Y. Zhao, F. Yang, R. Torrens, L. Bolzoni, Comparison of hot deformation behaviour and microstructural evolution for Ti-5Al-5V-5Mo-3Cr alloys prepared by powder metallurgy and ingot metallurgy approaches, Mater. Des. 169 (2019), 107682.
[53] D. Jia, W.R. Sun, D.S. Xu, F. Liu, Dynamic recrystallization behavior of GH4169G alloy during hot compressive deformation, J. Mater. Sci. Technol. 35 (2019) 1851–1859.